nature nanotechnology

Article

https://doi.org/10.1038/s41565-023-01451-x

Sign reversal of the Josephson inductance magnetochiral anisotropy and 0–π-like transitions in supercurrent diodes

Received: 29 December 2022

Accepted: 9 June 2023

Published online: 10 July 2023

Check for updates

A. Costa[1,8], C. Baumgartner[2,8], S. Reinhardt[2], J. Berger[2], S. Gronin[3], G. C. Gardner[3], T. Lindemann[3,4], M. J. Manfra[3,4,5,6], J. Fabian[1], D. Kochan[1,7], N. Paradiso[2] ✉ & C. Strunk[2]

The recent discovery of the intrinsic supercurrent diode effect, and its prompt observation in a rich variety of systems, has shown that non-reciprocal supercurrents naturally emerge when both space-inversion and time-inversion symmetries are broken. In Josephson junctions, non-reciprocal supercurrent can be conveniently described in terms of spin-split Andreev states. Here we demonstrate a sign reversal of the Josephson inductance magnetochiral anisotropy, a manifestation of the supercurrent diode effect. The asymmetry of the Josephson inductance as a function of the supercurrent allows us to probe the current–phase relation near equilibrium, and to probe jumps in the junction ground state. Using a minimal theoretical model, we can then link the sign reversal of the inductance magnetochiral anisotropy to the so-called 0–π-like transition, a predicted but still elusive feature of multichannel junctions. Our results demonstrate the potential of inductance measurements as sensitive probes of the fundamental properties of unconventional Josephson junctions.

Recent experiments[1–11] have shown that it is possible to obtain non-reciprocal supercurrents by acting solely on the spin degree of freedom of a superconductor through Zeeman fields. Since then, supercurrent rectifiers—called superconducting diodes—have generated keen interest due to their potential applications in dissipation-free electronics. From a fundamental point of view, the superconducting diode effect proved to be an important probe of symmetry breaking in novel and exotic superconducting systems, such as magic-angle twisted bilayer[12] or trilayer[13,14] graphene, as well as proximitized topological insulators[6,15,16].

The spin–orbit interaction (SOI) is the key ingredient to obtain supercurrent non-reciprocity through a Zeeman coupling, as first demonstrated for both bulk superconductors and Josephson junctions[2,3]. The phenomenology in both cases is similar: supercurrent rectification is induced by a Zeeman splitting of electron states with opposite momenta, which can happen in systems with spin–momentum locking due to the underlying SOI.

To date, theoretical models use different approaches to describe the supercurrent diode effect (SDE) in bulk superconductors and Josephson junctions. In the former case, non-reciprocity is usually attributed to the emergence of a helical phase[17–22], that is, to the finite Cooper-pair momentum that results from the SOI-split Fermi surface shifted due to Zeeman coupling. Instead, non-reciprocal supercurrent in superconducting–normal–superconducting (S–N–S) Josephson junctions is more conveniently described in terms of Andreev bound states[23–25] that, in the presence of Zeeman coupling and SOI, modify the

[1]Institut für Theoretische Physik, University of Regensburg, Regensburg, Germany. [2]Institut für Experimentelle und Angewandte Physik, University of Regensburg, Regensburg, Germany. [3]Birck Nanotechnology Center, Purdue University, West Lafayette, IN, USA. [4]Department of Physics and Astronomy, Purdue University, West Lafayette, IN, USA. [5]School of Materials Engineering, Purdue University, West Lafayette, IN, USA. [6]Elmore Family School of Electrical and Computer Engineering, Purdue University, West Lafayette, IN, USA. [7]Institute of Physics, Slovak Academy of Sciences, Bratislava, Slovakia. [8]These authors contributed equally: A. Costa, C. Baumgartner. ✉e-mail: nicola.paradiso@physik.uni-regensburg.de

current–phase relation (CPR) endowing it with an anomalous phase shift φ_0, with $\varphi_0 \neq 0, \pi$ (refs. 26–43). Such a phase shift leads to a marked asymmetry of the CPR, that is, $I(-\varphi) \neq -I(\varphi)$, where I is current. In the simplest case, the magnitude of φ_0 depends on the products of SOI and Zeeman coupling strengths, and on the inverse of the squared velocity of the impinging electrons (or holes)[28]. Since the latter is different for each transverse channel in the junction, the CPRs of individual channels acquire different φ_0 shifts (discussion in the Supplementary Information). The last ingredient necessary to obtain the diode effect is a skewed CPR, that is, a CPR with higher harmonics, as those observed in short-ballistic junctions. This requirement arises from the fact that the sum of different (also shifted) sine functions is still sinusoidal, and hence positive and negative critical currents have the same absolute value. Instead, the sum of skewed CPRs with different φ_0 shifts produces a distortion of the total CPR that breaks the symmetry between its positive and negative branches. We shall refer to the resulting difference between the positive and negative critical currents as the d.c. SDE. The asymmetry between positive and negative branches of the CPR also implies that its inflection point shifts to finite current i^*. Such an inflection point current corresponds to the minimum of the Josephson inductance L measured as a function of the current I. The finite i^* renders $L(I)$ asymmetric around $I = 0$, reflecting the magnetochiral anisotropy in the Josephson inductance[2]. Thus, the impedance for small a.c. signals will depend on the polarity of I, an effect that can be seen as the a.c. counterpart of the d.c. SDE.

In this work we demonstrate that large Rashba SOI together with a Zeeman field gives rise to a sign reversal of the inductance magnetochiral anisotropy (MCA) in ballistic multichannel Josephson junctions. We theoretically show that all experimental observations can be unambiguously explained by a minimal model linking the supercurrent flow to the underlying short-junction Andreev bound states. We demonstrate that the reversal of the inductance MCA naturally emerges as a consequence of the so-called 0–π-like transition, where the Josephson junction switches between two distinct minima of the corresponding energy–phase relation. Such transitions were predicted nearly a decade ago[37], but, to the best of our knowledge, not yet observed in experiments.

In our experiments we also observe that the d.c. SDE sharply peaks as a function of the in-plane magnetic field at a certain field value, and then it becomes rapidly suppressed at higher field values. With the help of our theoretical model, we can unambiguously explain both the reversal of the inductance MCA and the abrupt suppression of the d.c. SDE in terms of the intricate shape of the CPR in Rashba Josephson junctions under large in-plane fields.

Device and model description

We briefly describe our experiment, which is discussed in detail in the Methods as well as in our previous studies[2,44]. The starting point is a heterostructure featuring a very shallow InAs/InGaAs quantum well, hosting a two-dimensional electron gas (2DEG) with a large Rashba SOI. The heterostructure is capped by a 7-nm-thick epitaxial layer of Al, which induces superconductivity in the 2DEG by the proximity effect. By deep-etching, we define a mesa with a width of 3.15 μm for sample 1 and 3.27 μm for sample 3. By electron-beam lithography, we then selectively etch the Al film so that a gap of 100 nm is left between the adjacent pristine Al islands. We define an array of 2,250 islands, with a periodicity of 1.1 μm (refs. 2,44). In the top part of Fig. 1a, we sketch our device, showing only a few junctions for clarity. The reason why we work with long arrays and not with single junctions is merely technical and is discussed in the Supplementary Information. The 2DEG in the gap regions acts as a ballistic normal weak link connecting the superconducting 2DEG portions, in which the Al film induces a sizable gap $\Delta^* = 130$ μeV, that is, approximately 60% of that of the epitaxial Al (ref. 44). The transparency of our junctions is typically very high[44], with average transmission coefficients of $\bar{\tau} = 0.94$ for sample 1 and $\bar{\tau} = 0.93$ for sample 3. The array inductance is deduced from the resonance frequency shift of a resistor-inductor-capacitor (*RLC*) circuit, whose inductor is given by a Cu coil in series with the sample to be measured[2,44] (Methods).

In our theoretical model, a short, 2D S–N–S junction consists of two semi-infinite Rashba *s*-wave superconductors (S) phase-coherently coupled by a short non-superconducting (or normal; N) link (Fig. 1a, bottom). For simplicity, we consider the short-junction limit, which captures the Zeeman coupling due to the applied in-plane magnetic field and additionally introduces a small tunnelling potential to account for the non-perfect transparency of the junction. The Zeeman coupling is parameterized by $\lambda_Z = 2mV_Zd/(\hbar^2k_F)$, with the Zeeman potential V_Z, the effective electron mass m, the weak link thickness d, the 2DEG Fermi wave vector k_F and the reduced Planck's constant $\hbar$ (Methods). Magnetic field effects inside the bulk of the S regions (in particular the suppression of the proximity-induced superconducting gap with increasing magnetic field) are neglected.

Coherent Cooper-pair tunnelling through the S–N–S junction is mediated by Andreev bound states that are localized around the N link (Fig. 1a, bottom). To determine their energies and wavefunctions, we solve the stationary Bogoliubov–de Gennes equation[45]. From the Andreev spectrum we obtain the phase-asymmetric CPR, $I(\varphi)$, and consequently all the relevant quantities to be compared with the experimental data, namely, the polarity-dependent critical currents I_c^+ and I_c^-, and the Josephson inductance

$$L(I) = \frac{\hbar}{2e}\frac{\mathrm{d}\varphi(I)}{\mathrm{d}I}, \tag{1}$$

where e is the (positive) elementary charge.

Figure 1b illustrates the Josephson energy–phase relations, $E_J(\varphi)$, evaluated from our theoretical model for different values of the Zeeman parameter $\lambda_Z \in [0.5, 2.5]$. Note that the energy–phase relation in a multichannel system is given by $E_J(\varphi) = \Sigma_i\varepsilon_i(\varphi)$, where the sum runs over the individual transverse channels (i) with Andreev state energies ε_i. Our inductance measurements always probe the system in the vicinity of the global minimum of $E_J(\varphi)$, which is the experimental working point. Since the φ value at which $E_J(\varphi)$ is minimal is simultaneously a zero of $I(\varphi)$, such a phase, by definition, corresponds to the anomalous phase shift φ_0.

The main results of our analytical calculations (Fig. 1b) are that (1) $E_J(\varphi)$ features, at sufficiently high Zeeman fields λ_Z, two minima—one global and one local; and (2) when increasing λ_Z, the lower (global) minimum increases in energy, while the upper (local) minimum decreases, until a degeneracy point is reached where the system switches from one minimum (that is, from one anomalous phase $\varphi_{0,1}$) to the other ($\varphi_{0,2}$). In Fig. 1b, this transition occurs for $\lambda_Z = 1.94$ (black curve). Unlike for conventional 0–π transitions[46–50], the phase difference $\Delta\varphi \equiv |\varphi_{0,1} - \varphi_{0,2}|$ is appreciably less than π, owing to the anomalous phase shift φ_0. As discussed below, one experimental signature of this transition is the reversal of the inductance MCA.

Results and interpretation

Figure 2a shows our main experimental results, namely the in-plane field-induced reversal of the inductance MCA. In the graph, we report the Josephson inductance L as a function of the d.c. current I for different values of the in-plane magnetic field B_y, measured on sample 3. At moderate fields ($B_y < 200$ mT), the $L(I)$ curves are asymmetric around zero bias, with a minimum occurring at current $i^* < 0$, which corresponds to the inflection point of the CPR[2,44]. These minima are indicated by the open triangles in Fig. 2a.

Our central observation is the fact that at higher fields ($B_y > 200$ mT), the sign of i^* is inverted. By Taylor expansion of the $L(I)$ curves to the first order in I, we get two coefficients, that is, $L_0 \equiv L(0)$ and $L_0' \equiv \partial_I L(0)$, that as functions of the magnetic field serve as figures

https://doi.org/10.1038/s41565-023-01451-x

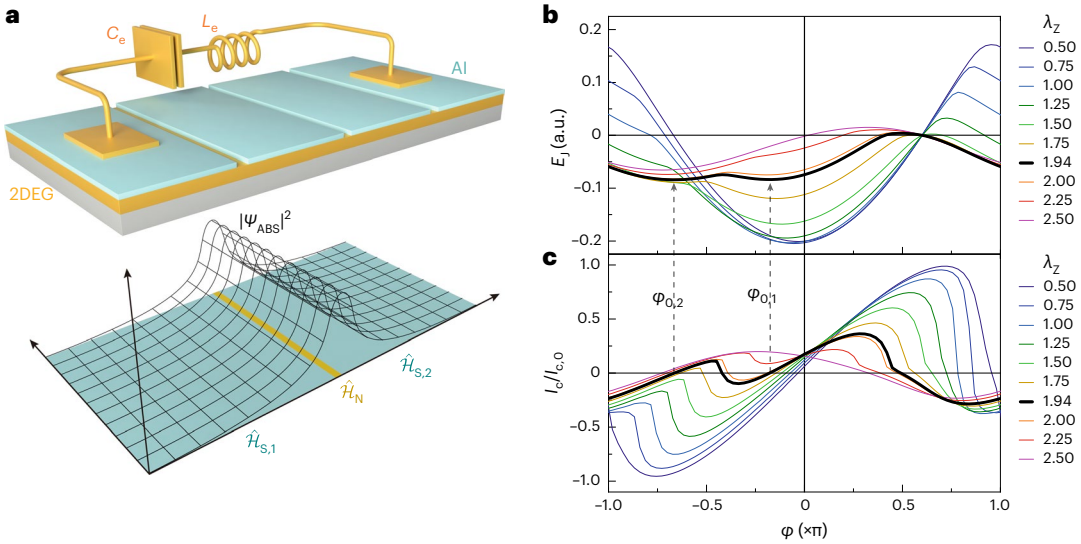

Fig. 1 | Multichannel Rashba Josephson junctions: experiment and theory. **a**, Sketch of the device, consisting of a one-dimensional (1D) Josephson junction array in series with an *LC* circuit (top). The external inductor has inductance L_e, while the external capacitor has conductance C_e. The superconducting regions consist of a 2DEG (yellow) proximitized by epitaxially grown Al islands (turquoise); they are connected through 2DEG weak links that are indicated by the gaps between the Al islands, as described in the main text. The theoretical model on the bottom shows that the two 2D Rashba superconductors (turquoise), described by the Hamiltonians $\hat{\mathcal{H}}_{S,1}$ and $\hat{\mathcal{H}}_{S,2}$, are connected by a delta-like N link (yellow) described by the Hamiltonian $\hat{\mathcal{H}}_N$ (Methods). The Andreev bound-state wavefunction Ψ_{ABS} (black lines show its absolute square) is strongly localized around the barrier. **b**, Computed Josephson energy as a function of the phase difference φ for various indicated Zeeman parameters λ_Z, as described in the text. Arrows indicate the positions of the two relevant energy minima, $\varphi_{0,2}$ and $\varphi_{0,1}$, which become degenerate at $\lambda_Z = 1.94$ (thick black curve) when the 0–π-like transition occurs. **c**, Computed current–phase relations for the Zeeman parameters considered in **b**; the current is normalized to the critical current at zero magnetic field, $I_{c,0} \equiv I_c(\lambda_Z = 0)$.

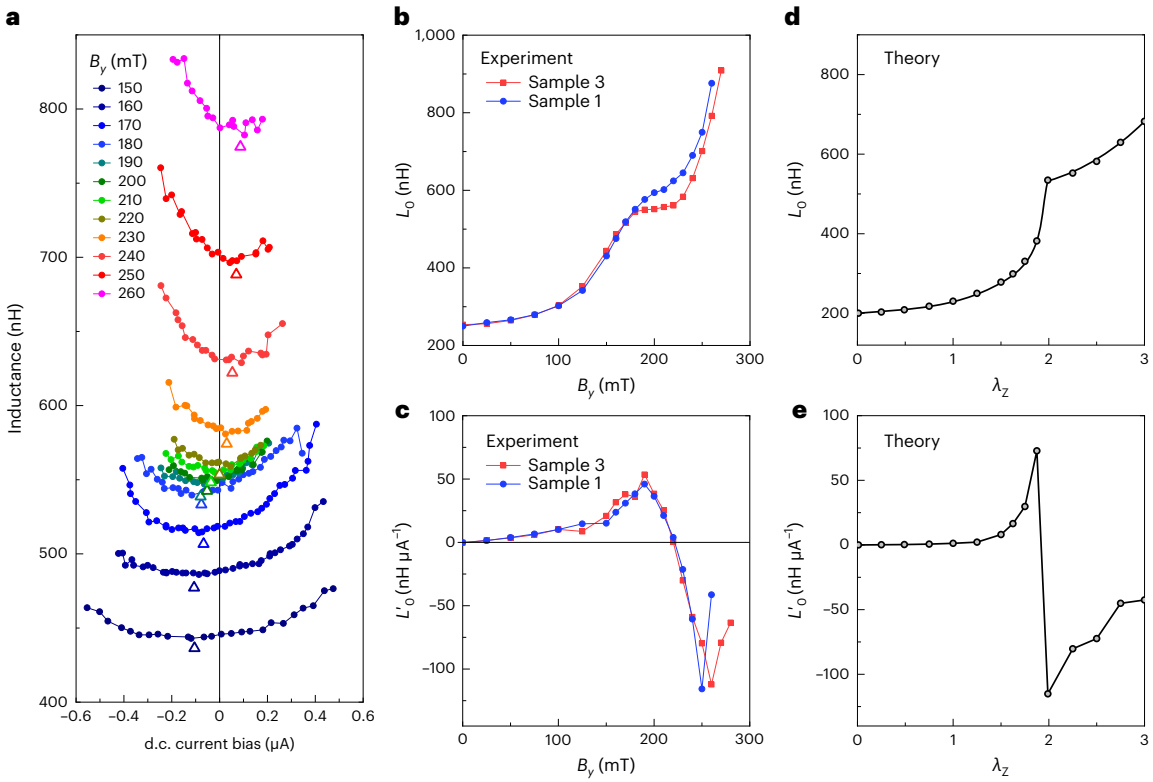

Fig. 2 | Reversal of the inductance MCA at the 0–π-like transition. **a**, Josephson inductance $L(I)$ for the array of sample 3, measured at temperature $T = 100$ mK as a function of the d.c. current I and for different values of the in-plane field component B_y perpendicular to the current. The open triangles indicate the current i^*, that is, the minimum of $L(I)$, as described in the text. **b**, Constant term L_0 of the polynomial expansion of $L(I)$, plotted versus B_y. **c**, Linear coefficient L'_0 of the polynomial expansion of $L(I)$, plotted versus B_y. Red (blue) symbols refer to sample 3 (sample 1). **d**, L_0 as computed from our theoretical model as a function of the phenomenological Zeeman parameter λ_Z. **e**, L'_0 as computed from our theoretical model as a function of λ_Z.

https://doi.org/10.1038/s41565-023-01451-x

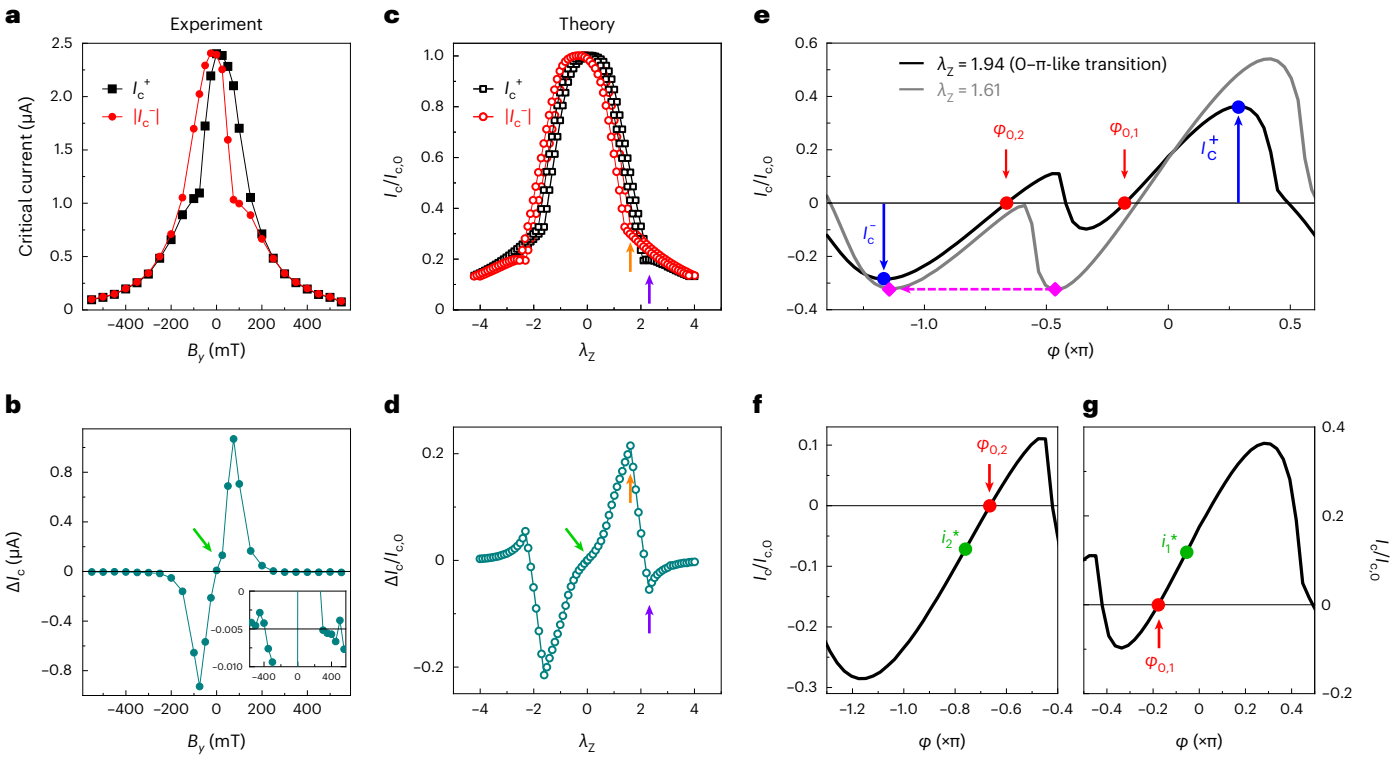

Fig. 3 | The d.c. SDE. a, Absolute value of the critical current measured on sample 1 for positive (I_c^+) and negative ($|I_c^-|$) bias, plotted as a function of the in-plane field B_y perpendicular to the current. **b**, Critical current difference $\Delta I_c = I_c^+ - |I_c^-|$. The inset shows a zoomed-in view with a reduced range in the vertical axis. **c**, I_c^+ and $|I_c^-|$ as computed from our theoretical model as a function of the phenomenological Zeeman parameter λ_Z. The critical current values are normalized to that for $\lambda_Z = 0$, that is, $I_{c,0} \equiv I_c(\lambda_Z = 0)$. For $\lambda_Z = 1.61$ (orange arrow) and $\lambda_Z = 2.31$ (purple arrow), two CPR minima and two CPR maxima become degenerate. This corresponds to a discontinuity in the slope of $|I_c^-(B_y)|$ and $I_c^+(B_y)$, respectively (more details in main text). **d**, Critical current difference $\Delta I_c(\lambda_Z)$ normalized to $I_{c,0}$, as deduced from **c**. The light green arrow indicates the zero-bias shoulder, as described in the main text, and the other arrows are as described in **c**. **e**, Computed CPR for $\lambda_Z = 1.94$ (black), corresponding to the 0–π-like transition in our model, and for $\lambda_Z = 1.61$ (grey), corresponding to the equality of the two minima of the CPR. For the $\lambda_Z = 1.94$ curve, red dots correspond to the anomalous phase shifts, while blue dots correspond to the absolute maximum and minimum of the CPR. For the $\lambda_Z = 1.61$ curve, the magenta arrow indicates the transition from one CPR minimum to another (magenta diamonds). **f**, Zoomed-in view near the second anomalous phase $\varphi_{0,2}$ for the $\lambda_Z = 1.94$ curve in **e**. The green dot indicates the first inflection point $i_2^* < 0$, which is a local minimum of the Josephson inductance $L(I)$. **g**, Zoomed-in view near the first anomalous phase $\varphi_{0,1}$ of the $\lambda_Z = 1.94$ curve in **e**. Note the opposite sign of i_1^* compared to i_2^*.

of merit of the inductance MCA[2]. In Fig. 2b,c, we show the B_y-field dependence of L_0 and L_0', respectively, for sample 3 (red symbols, corresponding to the data in Fig. 2a) and sample 1 (blue symbols). We notice that (1) the $L_0(B_y)$ curves feature a plateau at about 180 mT, corresponding to the accumulation of the $L(I)$ curves in Fig. 2a; (2) L_0' shows a nearly linear increase at low B_y fields followed by an upturn for $B_y > 100$ mT, with a peak at about 180 mT; and finally, (3) a dramatic drop with sign change occurs at $B_y = 220$ mT, reflecting the sign change of i^* in Fig. 2a, which is our main experimental finding.

Figure 2d,e shows the corresponding results of our theoretical calculations for $L_0(\lambda_Z)$ and $L_0'(\lambda_Z)$, respectively, as functions of λ_Z. Although our theoretical model treats the Zeeman coupling at the phenomenological level (through the single tunable parameter λ_Z), all relevant experimental observations from (1) to (3) are qualitatively reproduced. In particular, the plateau for L_0 and the L_0' peak followed by a sudden sign change are visible near $\lambda_Z = 2$ in Fig. 2d,e, respectively. In our calculations, both effects reflect the 0–π-like transition, where the anomalous phase switches from $\varphi_{0,1}$ to $\varphi_{0,2}$ (Fig. 1c). In the vicinity of $\varphi_{0,1}$ and $\varphi_{0,2}$, the sign of the CPR curvature (that is, $d^2I/d\varphi^2$) differs (Fig. 3e–g). Correspondingly, the sign of $L_0' \propto d^2\varphi/dI^2$ in the measurements changes as well.

Complementary to the inductance MCA is the d.c. SDE, that is, the polarity-dependent critical current. Figure 3a shows the B_y dependence of the critical current measured on sample 1 for the two bias polarities, namely, I_c^+ and $|I_c^-|$. We observe an evident critical current asymmetry, that is, a pronounced d.c. SDE. This can be better seen in Fig. 3b, where we plot the difference $\Delta I_c \equiv I_c^+ - |I_c^-|$. The main features of this graph are the nearly linear B_y dependence of ΔI_c up to 75 mT followed by a slope discontinuity and a sharp suppression of the rectification at higher values. Also, we notice a weak shoulder, barely visible near zero field (light green arrow in Fig. 3b,d). These characteristics of ΔI_c were already reported in the literature[2]. In the inset of Fig. 3b, we show a zoomed-in view of the $\Delta I_c(B_y)$ curve. We observe that ΔI_c converges to a finite value of −5 nA at high fields—for both $B_y > 0$ and $B_y < 0$—which we attribute to an instrumental offset. After subtracting this offset, we see that the graph of ΔI_c is point-symmetric around the origin, and it changes sign at $|B_y| \approx 400$ mT, before approaching zero. Such a sign change of the d.c. SDE is very weak, at the limit of the experimental visibility for the given data-point scatter, as opposed to the strong inversion of L_0' in Fig. 2c. It appears natural to ask what is the relation between the slope discontinuity of the d.c. SDE and the reversal of the inductance MCA displayed in Fig. 2.

The results of our analytical calculations help to clarify the origin of the slope discontinuity at $B_y = 75$ mT (−75 mT) for $|I_c^-|$ (I_c^+; Fig. 3a). Figure 3c presents the computed critical current for positive (I_c^+) and negative ($|I_c^-|$) bias as a function of the Zeeman parameter λ_Z, while Fig. 3d shows their respective difference ΔI_c. In both cases, the values are normalized to the critical current at $\lambda_Z = 0$. Despite its simplicity, the minimal model describes the main features of the experimental d.c. SDE, including the weak shoulder near $B_y = 0$. The computed ΔI_c

reaches a maximum at $\lambda_Z \approx 1.61$ (marked by the orange arrows in Fig. 3c,d) and experiences a discontinuous change in its slope that is followed by a steep descent to negative values. The slope of ΔI_c changes again at $\lambda_Z \approx 2.31$ (marked by the purple arrows in Fig. 3c,d), where the supercurrent rectification reaches its opposite maximum, before it eventually converges to zero at higher fields.

For an intuitive picture of the physical mechanism leading to the reversal of the d.c. SDE and inductance MCA, we need to look at the CPR in a large Zeeman field. In Fig. 3e, with the black curve, we display the computed CPR for $\lambda_Z = 1.94$, which corresponds to the 0–π-like transition. As discussed above (Fig. 1b,c), the unbiased system switches from the working point $\varphi_{0,1}$ to $\varphi_{0,2}$ at that value. For low current bias (as is the case for the inductance MCA experiments), the CPR probed near $\varphi_{0,1}$ is very different from that measured near $\varphi_{0,2}$, as shown in the zoomed-in graphs displayed in Fig. 3g,f, respectively. Both portions of the CPR are strongly asymmetric, but the magnitude and sign of the asymmetry are different. For instance, to reach the minimum of the $L(I)$ curve (namely, the inflection point i^* of the CPR), one needs to apply a positive current bias near $\varphi_{0,1}$ (Fig. 3g, green dot), whereas the bias must be negative to reach the inflection point near $\varphi_{0,2}$, that is, after the 0–π-like transition (Fig. 3f). In other words, the second derivatives (that is, the curvature) of the CPR in $\varphi_{0,1}$ and $\varphi_{0,2}$ have opposite signs. As a consequence, the computed $L_0' \propto d^2\varphi/dI^2$ must have a discontinuity at the 0–π-like transition, as observed in Fig. 2e.

As with the Josephson inductance MCA reversal, the sign change of the d.c. SDE originates from the complex shape of the CPR, which features two maxima and two minima at high in-plane fields. However, the experimental signature of the d.c. SDE sign change (i.e., the slope discontinuity for ΔI_c) does not occur exactly at the 0–π-like transition, that is, when the two minima of $E_J(\varphi)$ become degenerate. Instead, the d.c. SDE reversal is caused by the degeneracy of absolute maxima or minima of the CPR, as explained in the following. At small B_y fields, both the absolute maximum I_c^+ and the absolute minimum $|I_c^-|$ decrease with B_y, but the latter decreases faster (compare Figs. 1c and 3c), so that the difference ΔI_c increases with a nearly constant slope with B_y (compare Fig. 3a,c). At the in-plane field B_y corresponding to Zeeman coupling $\lambda_Z = 1.61$ (grey curve in Fig. 3e, below the 0–π-like transition), the two minima become degenerate. Eventually, for higher fields, I_c^- is determined by the new minimum (the one on the left in Fig. 3e, magenta arrow). The absolute value of this latter minimum decreases much more slowly with λ_Z, so that $|I_c^-|$ (and consequently ΔI_c) displays a slope discontinuity at $\lambda_Z = 1.61$ (orange arrow in Fig. 3c). For $\lambda_Z > 1.61$, I_c^+ decreases faster than $|I_c^-|$, until for $\lambda_Z = 2.14$ the two curves cross, that is, ΔI_c changes sign. In our model, we observe another slope discontinuity for $\lambda_Z = 2.31$ (purple arrow in Fig. 3c), corresponding to the degeneracy of two CPR maxima, which induces a negative peak in ΔI_c, followed by its suppression (Fig. 3d). In the experiment, owing to orbital pair breaking at high fields (ignored in the model), the visibility of such a negative peak is largely reduced (compare Fig. 3b,d). It is clear from our arguments that the sign reversal of ΔI_c is not directly related to the 0–π-like transition, although both phenomena originate from the complex character of the CPR in multichannel junctions. Our results might explain the often reported observation[2,3,7,8,51] of a sharp suppression of the d.c. SDE above a certain threshold field.

Discussion

Our findings demonstrate the importance of inductance experiments to extract information that is completely inaccessible in d.c. measurements. As opposed to the critical current, the inductance is a linear response observable that is accessible in the regime of small excitation, limited only by sensitivity. It is precisely this ability to probe the system near zero bias that allows us to reveal the 0–π-like transition by inductance measurements. Instead, under large d.c. bias, the critical current is determined by the absolute maximum (or minimum) of the CPR, and not by relative minima of the energy–phase relation, i.e, the working points. For this reason, 0–π-like transitions can hardly be observed in d.c. experiments on single junctions. Our theoretical calculations suggest that the reversal of the inductance MCA is much more pronounced than that of the d.c. SDE, precisely as observed in our experiments, emphasizing the great sensitivity of inductance measurements to probe the non-reciprocal supercurrent in Josephson junctions.

It is important to mention that experiments on $NiTe_2$ junctions[6] have shown multiple oscillations of the d.c. SDE, with ΔI_c appearing as a damped sine function of the in-plane field. By contrast, our experimental data, as well as experiments in the literature[8,51], are not compatible with a (damped) sinusoidal dependence: the cusp-like change of the ΔI_c slope at $B_y = 75$ mT in our experiment can certainly not be reproduced by a damped sine.

Finally, we would like to stress that asymmetric vortex barriers, which have recently been invoked to explain supercurrent rectification effects in plain superconducting films[52,53], as well as in epitaxial Al/InAs bilayers[54], do not seem to play any important role in our experiments, where both the critical current and inductance are completely determined by only the Josephson junction properties.

Conclusions

In conclusion, we experimentally demonstrate a sign change of the inductance MCA in ballistic Josephson junctions with a large Rashba SOI. Based on a minimal theoretical model, we show that this effect provides an experimental signature of 0–π-like transitions in the CPR. The model predicts a slope discontinuity in the critical current difference versus in-plane field, followed eventually by a sign change of the d.c. diode effect. The former effect is clearly visible in the experiment, while the latter is below the limit of visibility. The phenomena studied here originate from the distinct spectral properties of the Andreev bound states corresponding to different transverse channels. The sum of their contribution gives rise to a complex Josephson energy landscape, resulting from the different anomalous φ_0 shifts for the individual transverse channels.

Supercurrent non-reciprocity is a valuable probe of the physics of Josepshon junctions in systems with broken inversion and time-reversal symmetries. As proposed in a recent work[55], the SDE can be used to detect topological phase transitions in a way that is protected from parity-altering events such as quasiparticle poisoning.

From a technological perspective, supercurrent diodes are promising building blocks for fully superconducting electronics for quantum computing applications. In fact, a non-zero L_0' is a key element[56] of recently proposed non-reciprocal radiofrequency devices[57]. Until now, a finite effective L_0' could only be engineered via complex superconducting quantum interference devices (SQUIDs)[58]. Here we show that it is instead a robust feature of single Rashba Josephson junctions.

We note that during the review process, we became aware of two related works[59,60] investigating the same type of junctions studied here, which appeared after the submission of the present manuscript. One study[59] reports asymmetric Andreev spectra measured in the same type of junction we studied. The other[60] relates the reversal of the d.c. SDE to the length of the superconducting leads, which might explain the weakness of the d.c. SDE reversal we measured.

Online content

Any methods, additional references, Nature Portfolio reporting summaries, source data, extended data, supplementary information, acknowledgements, peer review information; details of author contributions and competing interests; and statements of data and code availability are available at https://doi.org/10.1038/s41565-023-01451-x.

References

1. Ando, F. et al. Observation of superconducting diode effect. *Nature* **584**, 373–376 (2020).

2. Baumgartner, C. et al. Supercurrent rectification and magnetochiral effects in symmetric Josephson junctions. *Nat. Nanotechnol.* **17**, 39–44 (2022).
3. Baumgartner, C. et al. Effect of Rashba and Dresselhaus spin–orbit coupling on supercurrent rectification and magnetochiral anisotropy of ballistic Josephson junctions. *J. Phys. Condens. Matter* **34**, 154005 (2022).
4. Wu, H. et al. The field-free Josephson diode in a van der Waals heterostructure. *Nature* **604**, 653–656 (2022).
5. Jeon, K.-R. et al. Zero-field polarity-reversible Josephson supercurrent diodes enabled by a proximity-magnetized Pt barrier. *Nat. Mater.* **21**, 1008–1013 (2022).
6. Pal, B. et al. Josephson diode effect from Cooper pair momentum in a topological semimetal. *Nat. Phys.* https://doi.org/10.1038/s41567-022-01699-5 (2022).
7. Bauriedl, L. et al. Supercurrent diode effect and magnetochiral anisotropy in few-layer $NbSe_2$. *Nat. Commun.* **13**, 4266 (2022).
8. Turini, B. et al. Josephson diode effect in high-mobility InSb nanoflags. *Nano Lett.* **22**, 8502–8508 (2022).
9. Gupta, M. et al. Gate-tunable superconducting diode effect in a three-terminal Josephson device. *Nat. Commun.* **14**, 3078 (2023).
10. Zhang, B. et al. Evidence of φ0-Josephson junction from skewed diffraction patterns in Sn-InSb nanowires. Preprint at *arXiv* https://doi.org/10.48550/arXiv.2212.00199 (2022).
11. Mazur, G. P. et al. The gate-tunable Josephson diode. Preprint at *arXiv* https://doi.org/10.48550/arXiv.2211.14283 (2022).
12. Diez-Merida, J. et al. Symmetry-broken Josephson junctions and superconducting diodes in magic-angle twisted bilayer graphene. *Nat. Commun.* **14**, 2396 (2023).
13. Lin, J.-X. et al. Zero-field superconducting diode effect in small-twist-angle trilayer graphene. *Nat. Phys.* **18**, 1221–1227 (2022).
14. Scammell, H. D., Li, J. I. A. & Scheurer, M. S. Theory of zero-field superconducting diode effect in twisted trilayer graphene. *2D Mater.* **9**, 025027 (2022).
15. Lu, B., Ikegaya, S., Burset, P., Tanaka, Y. & Nagaosa, N. Josephson diode effect on the surface of topological insulators. Preprint at *arXiv* https://doi.org/10.48550/arXiv.2211.10572 (2022).
16. Fu, P.-H., Xu, Y., Lee, C. H., Ang, Y. S. & Liu, J.-F. Gate-tunable high-efficiency topological Josephson diode. Preprint at *arXiv* https://doi.org/10.48550/arXiv.2212.01980 (2022).
17. Daido, A., Ikeda, Y. & Yanase, Y. Intrinsic superconducting diode effect. *Phys. Rev. Lett.* **128**, 037001 (2022).
18. Yuan, N. F. Q. & Fu, L. Supercurrent diode effect and finite-momentum superconductors. *Proc. Natl Acad. Sci. USA* **119**, e2119548119 (2022).
19. He, J. J., Tanaka, Y. & Nagaosa, N. A phenomenological theory of superconductor diodes. *New J. Phys.* **24**, 053014 (2022).
20. Ilić, S. & Bergeret, F. S. Theory of the supercurrent diode effect in Rashba superconductors with arbitrary disorder. *Phys. Rev. Lett.* **128**, 177001 (2022).
21. Legg, H. F., Loss, D. & Klinovaja, J. Superconducting diode effect due to magnetochiral anisotropy in topological insulators and rashba nanowires. *Phys. Rev. B* **106**, 104501 (2022).
22. Kochan, D., Costa, A., Zhumagulov, I. and Žutić, I. Phenomenological theory of the supercurrent diode effect: the Lifshitz invariant. Preprint at *arXiv* https://doi.org/10.48550/arXiv.2303.11975 (2023).
23. Andreev, A. F. Electron spectrum of the intermediate state of superconductors. *Zh. Eksp. Teor. Fiz.* **49**, 655 (1966). *J. Exp. Theor. Phys.* **22**, 455–458 (1966).
24. Davydova, M., Prembabu, S. & and Fu, L. Universal Josephson diode effect. *Sci. Adv.* **8**, eabo0309 (2022).
25. Grein, R., Eschrig, M., Metalidis, G. & Schön, G. Spin-dependent Cooper pair phase and pure spin supercurrents in strongly polarized ferromagnets. *Phys. Rev. Lett.* **102**, 227005 (2009).
26. Bezuglyi, E. V., Rozhavsky, A. S., Vagner, I. D. & Wyder, P. Combined effect of Zeeman splitting and spin-orbit interaction on the Josephson current in a superconductor–two-dimensional electron gas–superconductor structure. *Phys. Rev. B* **66**, 052508 (2002).
27. Krive, I. V., Gorelik, L. Y., Shekhter, R. I. & Jonson, M. Chiral symmetry breaking and the Josephson current in a ballistic superconductor–quantum wire–superconductor junction. *Low. Temp. Phys.* **30**, 398–404 (2004).
28. Buzdin, A. Direct coupling between magnetism and superconducting current in the Josephson φ_0 junction. *Phys. Rev. Lett.* **101**, 107005 (2008).
29. Reynoso, A. A., Usaj, G., Balseiro, C. A., Feinberg, D. & Avignon, M. Anomalous Josephson current in junctions with spin polarizing quantum point contacts. *Phys. Rev. Lett.* **101**, 107001 (2008).
30. Zazunov, A., Egger, R., Jonckheere, T. & Martin, T. Anomalous Josephson current through a spin-orbit coupled quantum dot. *Phys. Rev. Lett.* **103**, 147004 (2009).
31. Liu, J.-F. & Chan, K. S. Relation between symmetry breaking and the anomalous Josephson effect. *Phys. Rev. B* **82**, 125305 (2010).
32. Liu, J.-F. & Chan, K. S. Anomalous Josephson current through a ferromagnetic trilayer junction. *Phys. Rev. B* **82**, 184533 (2010).
33. Liu, J.-F., Chan, K. S. & Wang, J. Anomalous Josephson current through a ferromagnet-semiconductor hybrid structure. *J. Phys. Soc. Jpn* **80**, 124708 (2011).
34. Reynoso, A. A., Usaj, G., Balseiro, C. A., Feinberg, D. & Avignon, M. Spin-orbit-induced chirality of Andreev states in Josephson junctions. *Phys. Rev. B* **86**, 214519 (2012).
35. Yokoyama, T., Eto, M. & Nazarov, Y. V. Josephson current through semiconductor nanowire with spin–orbit interaction in magnetic field. *J. Phys. Soc. Jpn* **82**, 054703 (2013).
36. Brunetti, A., Zazunov, A., Kundu, A. & Egger, R. Anomalous Josephson current, incipient time-reversal symmetry breaking, and Majorana bound states in interacting multilevel dots. *Phys. Rev. B* **88**, 144515 (2013).
37. Yokoyama, T., Eto, M. & Nazarov, Y. V. Anomalous Josephson effect induced by spin-orbit interaction and Zeeman effect in semiconductor nanowires. *Phys. Rev. B* **89**, 195407 (2014).
38. Shen, K., Vignale, G. & Raimondi, R. Microscopic theory of the inverse Edelstein effect. *Phys. Rev. Lett.* **112**, 096601 (2014).
39. Konschelle, F., Tokatly, I. V. & Bergeret, F. S. Theory of the spin-galvanic effect and the anomalous phase shift φ_0 in superconductors and Josephson junctions with intrinsic spin-orbit coupling. *Phys. Rev. B* **92**, 125443 (2015).
40. Szombati, D. B. et al. Josephson φ_0-junction in nanowire quantum dots. *Nat. Phys.* **12**, 568–572 (2016).
41. Assouline, A. et al. Spin-orbit induced phase-shift in Bi_2Se_3 Josephson junctions. *Nat. Commun.* **10**, 126 (2019).
42. Mayer, W. et al. Gate controlled anomalous phase shift in Al/InAs Josephson junctions. *Nat. Commun.* **11**, 212 (2020).
43. Strambini, E. et al. A Josephson phase battery. *Nat. Nanotechnol.* **15**, 656–660 (2020).
44. Baumgartner, C. et al. Josephson inductance as a probe for highly ballistic semiconductor-superconductor weak links. *Phys. Rev. Lett.* **126**, 037001 (2021).
45. De Gennes, P. G. *Superconductivity of Metals and Alloys* (Addison Wesley, 1989).
46. Li, C. et al. Zeeman-effect-induced 0–π transitions in ballistic Dirac semimetal Josephson junctions. *Phys. Rev. Lett.* **123**, 026802 (2019).
47. Hart, S. et al. Controlled finite momentum pairing and spatially varying order parameter in proximitized HgTe quantum wells. *Nat. Phys.* **13**, 87–93 (2017).
48. Chen, A. Q. et al. Finite momentum Cooper pairing in three-dimensional topological insulator Josephson junctions. *Nat. Commun.* **9**, 3478 (2018).

49. Ke, C. T. et al. Ballistic superconductivity and tunable π–junctions in InSb quantum wells. *Nat. Commun.* **10**, 3764 (2019).
50. Whiticar, A. M. et al. Zeeman-driven parity transitions in an Andreev quantum dot. *Phys. Rev. B* **103**, 245308 (2021).
51. Shin, J. et al. Magnetic proximity-induced superconducting diode effect and infinite magnetoresistance in a van der Waals heterostructure. *Phys. Rev. Res.* **5**, L022064 (2023).
52. Hou, Y. et al. Ubiquitous superconducting diode effect in superconductor thin films. Preprint at *arXiv* https://doi.org/10.48550/arXiv.2205.09276 (2022).
53. Suri, D. et al. Non-reciprocity of vortex-limited critical current in conventional superconducting micro-bridges. *Appl. Phys. Lett.* **121**, 102601 (2022).
54. Sundaresh, A., Vayrynen, J. I., Lyanda-Geller, Y. & Rokhinson, L. P. Diamagnetic mechanism of critical current non-reciprocity in multilayered superconductors. *Nat. Commun.* **14**, 1628 (2023).
55. Legg, H. F., Laubscher, K., Loss, D. & Klinovaja, J. Parity protected superconducting diode effect in topological Josephson junctions. Preprint at *arXiv* https://doi.org/10.48550/arXiv.2301.13740 (2023).
56. Frattini, N. E. et al. 3-wave mixing Josephson dipole element. *Appl. Phys. Lett.* **110**, 222603 (2017).
57. Leroux, C. et al. Nonreciprocal devices based on voltage-tunable junctions. Preprint at *arXiv* https://doi.org/10.48550/arXiv.2209.06194 (2022).
58. Roudsari, A. F. et al. Three-wave mixing traveling-wave parametric amplifier with periodic variation of the circuit parameters. *Appl. Phys. Lett.* **122**, 052601 (2023).
59. Banerjee, A. et al. Phase asymmetry of Andreev spectra from Cooper-pair momentum. Preprint at *arXiv* https://doi.org/10.48550/arXiv.2301.01881 (2023).
60. Lotfizadeh, N. et al. Superconducting diode effect sign change in epitaxial Al-InAs Josepshon junctions. Preprint at *arXiv* https://doi.org/10.48550/arXiv.2303.01902 (2023).

Methods

Experimental details

Samples are fabricated starting from a semiconductor/metal heterostructure grown by molecular-beam epitaxy. The topmost layer (Al, 7 nm) is separated by a quantum well ($In_{0.81}Ga_{0.19}As$, 4 nm; InAs, 7 nm; $In_{0.80}Ga_{0.20}As$, 10 nm) by two monolayers of GaAs. The quantum well hosts a 2DEG with density $n = 5 \times 10^{11}$ cm^{-2} and mobility of approximately $\mu = 2.2 \times 10^4$ cm^2 V^{-1} s^{-1}. The Josephson junction array is defined on a mesa structure, fabricated via electron-beam lithography followed by a wet-etching step. Then, to obtain the weak links, we remove the topmost Al layer by electron-beam lithography followed by highly selective Al wet-etching. The selectivity of the etching is crucial to obtain ballistic junctions with high transparency. Further details about the sample structure and fabrication are provided in ref. 44.

To measure both the inductance and d.c. transport characteristics, we embed the sample under study in a circuit featuring an *RLC* resonator in series with the sample. The circuit is mounted on the sample holder thermally anchored to the cold finger of a dilution refrigerator. Four leads make possible d.c. transport measurements in a four-terminal configuration. The four leads are connected to the cryostat lines via 1 kΩ decoupling resistors. The inductance and capacitance of the *RLC* resonator are $L_e = 382$ nH and $C_e = 4$ nF, respectively. The resonance frequency for negligible contribution from the sample is, therefore, $f_0 = 4$ MHz. The inductance of the sample is deduced from the reduction of the resonance frequency with respect to f_0. More details on the circuit can be found in the Supplementary Information and in ref. 44.

Details of the theoretical model

Our minimal theoretical model allows us to relate the supercurrent of a short-ballistic multichannel Josephson junction with the spectral properties of the associated Andreev bound states. Based on these properties, we explain the experimentally observed d.c. SDE and inductance MCA. Assuming that all 2,250 junctions within the array are identical, we focus on one single S–N–S junction, and extract its Josephson CPR, its Josephson energy and thus the Josephson inductance—the inductance of the whole array is just a multiple of 2,250 of the latter.

We model the short S–N–S junction as two semi-infinite superconducting (S) leads that are phase-coherently coupled by a delta-like normal (N) link (Fig. 1, bottom). The coherent transport of Cooper pairs through the junction is mediated by Andreev bound states, whose energies and wavefunctions are obtained by solving the stationary 2D Bogoliubov–de Gennes equation[45] with eigenfunction $\Psi(x,y)$ and eigenvalue E

$$\begin{bmatrix} \hat{\mathcal{H}} & \hat{\Delta}(x) \\ \hat{\Delta}^\dagger(x) & -\hat{\sigma}_y(\hat{\mathcal{H}})^*\hat{\sigma}_y \end{bmatrix} \Psi(x,y) = E\Psi(x,y), \tag{2}$$

where the single-electron Hamiltonian reads as

$$\hat{\mathcal{H}} = \hat{\mathcal{H}}_{S,1}\,\Theta(-x) + \hat{\mathcal{H}}_{S,2}\,\Theta(x) + \hat{\mathcal{H}}_N\,\delta(x), \tag{3}$$

with

$$\hat{\mathcal{H}}_{S,1/2} = \left[-\frac{\hbar^2}{2m}\left(\frac{\partial^2}{\partial x^2} + \frac{\partial^2}{\partial y^2}\right) - \mu\right]\hat{\sigma}_0 + \alpha\left(k_y\hat{\sigma}_x - k_x\hat{\sigma}_y\right) \tag{4}$$

and

$$\hat{\mathcal{H}}_N = \left(V_0\,\hat{\sigma}_0 + V_Z\,\hat{\sigma}_y\right)d. \tag{5}$$

In the above expressions, $\hat{\Delta}(x)$ is the pairing potential, $\delta(x)$ and $\Theta(x)$ are the Dirac and the Heaviside function, α parameterizes the Rashba SOI that is present throughout the whole junction, k_x (k_y) is the wavevector along the x (y) direction and V_Z and V_0 stand for the heights of the Zeeman and scalar (spin-independent) potentials that are spreading over the full width of the N weak link with effective length d. While V_Z takes care about the in-plane magnetic field (aligned along the $\hat{y}$ axis) that couples to spin via the Zeeman coupling, the reason to introduce V_0 is merely to capture a reduced transparency of the N link, caused, for example, by different electronic densities in the proximitized S and N regions[61]. Moreover, m denotes the effective (quasiparticle) mass; $\mu = \hbar^2 k_F^2/(2m)$, the Fermi energy; $\hat{\sigma}_0$, the 2 × 2 identity matrix; and $\hat{\sigma}_x$ and $\hat{\sigma}_y$ stand for the Pauli matrices.

The s-wave superconducting pairing potential (induced by the epitaxially grown Al layer) can be written as

$$\hat{\Delta}(x) = \Delta^*\left[\Theta(-x) + e^{i\varphi}\Theta(x)\right], \tag{6}$$

where i is the imaginary unit, Δ^* is the proximity-induced superconducting gap and φ is the superconducting phase difference along the junction.

To find the Andreev bound states, we (1) start with the most general ansatz for the in-gap (bound-state) wavefunctions in the superconductors, (2) then eliminate all unknown amplitudes that enter this ansatz by applying appropriate boundary conditions that should be satisfied at the N interface and (3) request the final system of algebraic equations to have a non-trivial solution to get a secular equation. We solve the latter obtaining the Andreev bound-state energies, and subsequently also the unknown amplitudes, which gives us the bound-state wavefunctions in real space. Having the wavefunctions, we compute the expectation values of the current operator in the N region, which is equal to the Josephson current due to charge conservation—so the Cooper-pair tunnelling is mediated by the available Andreev bound states. Varying the superconducting phase difference φ, we finally recover the Josephson CPR $I(\varphi)$, the direction-dependent critical currents I_c^+ and I_c^- and the Josephson inductance

$$L(I) = \frac{\hbar}{2e}\frac{\mathrm{d}\varphi(I)}{\mathrm{d}I}, \tag{7}$$

which we compare with the experimental data; e refers to the (positive) elementary charge.

To shorten the notation, we define the dimensionless parameters $\lambda_{SOI} = m\alpha/(\hbar^2 k_F)$, $Z = 2mV_0 d/(\hbar^2 k_F)$ and $\lambda_Z = 2mV_Z d/(\hbar^2 k_F)$ to quantify the Rashba SOI, the strength of the (scalar) barrier and the strength of the Zeeman coupling, respectively. In agreement with our earlier experimental findings[44], we set $Z = 0.5$ in all calculations, which corresponds to a junction transparency[62] of $\bar{\tau} = 1/[1 + (Z/2)^2] \approx 0.94$, whereas the Rashba SOI $\lambda_{SOI} = 0.661$ was adapted such that varying the phenomenological Zeeman parameter λ_Z reproduces at best the qualitative magnetic field dependence of the experimental data.

Although our minimal model includes the Zeeman coupling only in a delta-like manner, we can still exploit the formal analogy with a realistic Zeeman Hamiltonian to convert λ_Z into a plausible value for the experimental magnetic field. Substituting the formula for the Zeeman gap, $V_Z = |g^*|\mu_B B_y/2$, where[2] $|g^*| \approx 10$ and μ_B denotes the Bohr magneton, into the above definition of λ_Z, the corresponding magnetic field is $B_y = [\hbar^2 k_F/(m|g^*|\mu_B d)] \times \lambda_Z$. For a typical Fermi wave vector of $k_F \approx 3 \times 10^8$ m^{-1} and N link length of $d = 100$ nm, the 0–π-like transition point at $\lambda_Z \approx 2$ in our model refers then to a magnetic field of $B_y \approx 800$ mT. This estimate also agrees reasonably well with the transition field observed in the literature[63]. What matters to map theory and experiment is the elevated ratio of SOI strength to Fermi level, which in our case reads $\alpha k_F/\mu = 2\lambda_{SOI} \approx 1.2$.

In the experiment, the 0–π-like transition occurs already at a substantially smaller magnetic field of about 200 mT (Fig. 2c). The reason for this quantitative discrepancy between experiment and theory is most likely the neglect of gap-suppression effects inside the superconducting regions in our theory, as well as the too coarse approximation

of the N link by means of a simple delta function. Extracting the field dependence of the proximity-induced superconducting gap, $\Delta^*(B_y)$, from the experimental inductance data indeed confirms that the gap becomes substantially suppressed and the Zeeman energy can already overcome the superconducting gap at about 200 mT. As a consequence, the superconducting gap essentially closes for one spin channel, and the junction undergoes the 0–π-like transition.

Data availability

The data that support the findings of this study are available at the online depository EPUB of the University of Regensburg, with the identifier https://doi.org/10.5283/epub.53466. Source data are provided with this paper.

Code availability

The computer codes that support the theoretical results, the plots within this paper and other findings of this study are available from the corresponding author upon reasonable request.

References

61. Žutić, I. & Valls, O. T. Tunneling spectroscopy for ferromagnet/superconductor junctions. *Phys. Rev. B* **61**, 1555–1566 (2000).
62. Blonder, G. E., Tinkham, M. & Klapwijk, T. M. Transition from metallic to tunneling regimes in superconducting microconstrictions: excess current, charge imbalance, and supercurrent conversion. *Phys. Rev. B* **25**, 4515–4532 (1982).
63. Dartiailh, M. C. et al. Phase signature of topological transition in Josephson junctions. *Phys. Rev. Lett.* **126**, 036802 (2021).

Acknowledgements

Work at Regensburg University was funded by the Deutsche Forschungsgemeinschaft (DFG, German Research Foundation) through project no. 314695032 (SFB 1277 (subprojects B05, B07 and B08)) and project no. 454646522, research grant 'Spin and magnetic properties of superconducting tunnel junctions' (A.C. and J.F.). D.K. acknowledges partial support from the project IM-2021-26 (SUPERSPIN) funded by the Slovak Academy of Sciences via the programme IMPULZ 2021.

Author contributions

C.B. and J.B. fabricated the devices and performed the measurements. A.C. performed the numerical simulations. A.C., D.K. and J.F. formulated the theoretical model. S.R. developed and optimized the measurement method. T.L., S.G. and G.C.G. designed the heterostructure, conducted molecular-beam epitaxy growth and performed the initial characterization of the hybrid superconductor/semiconductor wafer. C.B. and N.P. analysed the data. N.P. and C.S. conceived the experiment. C.S. and M.J.M. supervised research activities at Regensburg and Purdue, respectively. N.P., A.C. and D.K. wrote the manuscript. All authors contributed to discussions and to the refinement of the manuscript.

Competing interests

The authors declare no competing interests.

Additional information

Supplementary information The online version contains supplementary material available at https://doi.org/10.1038/s41565-023-01451-x.

Correspondence and requests for materials should be addressed to N. Paradiso.

Peer review information *Nature Nanotechnology* thanks Mathias Scheurer, Elia Strambini and the other, anonymous, reviewer(s) for their contribution to the peer review of this work.